Simultaneous spatiotemporal tracking and oxygen sensing of transient implants in vivo using hot-spot MRI and machine learning

Virginia Spanoudaki[a,b], Joshua C. Doloff[a,b,c,1], Wei Huang[a], Samuel R. Norcross[a,b], Shady Farah[a,b,c], Robert Langer[a,b,c,d,e], and Daniel G. Anderson[a,b,c,d,e,2]

[a]David H Koch Institute for Integrative Cancer Research, Massachusetts Institute of Technology, Cambridge, MA 02139; [b]Department of Anesthesiology, Boston Children's Hospital, Harvard Medical School, Boston, MA 02115; [c]Department of Chemical Engineering, Massachusetts Institute of Technology, Cambridge, MA 02139; [d]Division of Health Science Technology, Massachusetts Institute of Technology, Cambridge, MA 02139; and [e]Institute for Medical Engineering and Science, Massachusetts Institute of Technology, Cambridge, MA 02139

Edited by John A. Rogers, Northwestern University, Evanston, IL, and approved January 23, 2019 (received for review September 18, 2018)

A varying oxygen environment is known to affect cellular function in disease as well as activity of various therapeutics. For transient structures, whether they are unconstrained therapeutic transplants, migrating cells during tumor metastasis, or cell populations induced by an immunological response, the role of oxygen in their fate and function is known to be pivotal albeit not well understood in vivo. To address such a challenge in the case of generation of a bioartificial pancreas, we have combined fluorine magnetic resonance imaging and unsupervised machine learning to monitor over time the spatial arrangement and the oxygen content of implants encapsulating pancreatic islets that are unconstrained in the intraperitoneal (IP) space of healthy and diabetic mice. Statistically significant trends in the postimplantation temporal dependence of oxygen content between aggregates of 0.5-mm or 1.5-mm alginate microcapsules were identified in vivo by looking at their dispersity as well as arrangement in clusters of different size and estimating oxygen content on a pixel-by-pixel basis from thousands of 2D images. Ultimately, we found that this dependence is stronger for decreased implant capsule size consistent with their tendency to also induce a larger immunological response. Beyond the bioartificial pancreas, this work provides a framework for the simultaneous spatiotemporal tracking and oxygen sensing of other cell populations and biomaterials that change over time to better understand and improve therapeutic design across diverse applications such as cellular transplant therapy, treatments preventing metastatic formation, and modulators for improving immunologic response, for all of which oxygen is a major mechanistic component.

magnetic resonance imaging | oxygen sensing | cellular therapy | diabetes | implants

The question of how oxygen conditions affect the fate and function of cells is of great interest for the understanding of the underlying mechanisms of disease such as cancer (1), in immunology (2), as well as in the development of therapeutics (3). Furthermore, when these conditions are transient in nature, as is often the case in vivo, their monitoring becomes a challenge. In vitro assays have produced a large body of knowledge with diverse conclusions, in large part because the actual physiologic conditions that cells encounter within a complex biological system cannot be adequately replicated in vitro. Intravital microscopy techniques overcome this limitation; however, they are not able to produce pure volumetric information (4) which is often needed to identify spatially dependent trends. In vivo volumetric imaging techniques that are able to track shifting cell populations and therapeutic materials have recently emerged (5), with MRI offering a satisfactory trade-off between sensitivity and spatial resolution (6, 7). In this study we develop approaches to examine the ability of this imaging modality to both track implanted materials volumetrically and probe their oxygen content under transient conditions for deeper understanding in the case of the bioartificial pancreas.

Cellular transplants of pancreatic islets hold the promise of providing diabetic patients with a controlled, long-term release of insulin without the need of external pumps and monitors (8, 9). Significant progress has been made in the development and investigation of biocompatible encapsulation materials that protect islet allografts from the host's immune response, while at the same time allowing the influx of oxygen and nutrients to the cells and the delivery of insulin to the host (10, 11). Chemical modification of the encapsulation materials (12) or their geometrical features, such as their size and shape (13), plays an important role in the fibrotic response and long-term efficacy of biomaterial encapsulated cellular transplants. Recently, long-term glycemic control in immunocompetent mice using encapsulated stem-cell–derived beta-like cells has been reported (14).

Due to the ease of laparoscopic procedures, the peritoneal cavity [or intraperitoneal (IP) space] is a typical implantation site for encapsulated islets (15, 16). Importantly, this site offers a large enough space to hold a curative transplant biomass (17).

Significance

In this work we performed long-term, time and spatially resolved in vivo position and oxygen sensing of differently sized biomaterial implants that are transient and moving in the intraperitoneal space. Prior studies of biomaterial oxygenation using imaging have been limited to fixed, defined implantation areas with no consideration regarding how the material environment changes over time. In this study, we derived associations between changes in the spatial arrangement of the implants and their oxygen content by using unsupervised machine-learning clustering algorithms that screened for patterns over thousands of 2D images. The methodology presented here can be used to guide more efficient design of cellular transplants where proper oxygenation is of utmost importance for therapeutic efficacy.

Author contributions: V.S., R.L., and D.G.A. designed research; V.S., W.H., S.R.N., and S.F. performed research; V.S. and J.C.D. contributed new reagents/analytic tools; V.S., J.C.D., and S.R.N. analyzed data; and V.S. wrote the paper.

Conflict of interest statement: D.G.A. and R.L. are founding scientists of Sigilon Therapeutics, a biotech company based in Cambridge, MA.

This article is a PNAS Direct Submission.

[1]Present addresses: Departments of Biomedical and Materials Science Engineering, Translational Tissue Engineering Center, Wilmer Eye Institute, and the Institute for NanoBioTechnology, Johns Hopkins University School of Medicine, Baltimore, MD 21231.

[2]To whom correspondence should be addressed. Email: dgander@mit.edu.

This article contains supporting information online at www.pnas.org/lookup/suppl/doi:10.1073/pnas.1815909116/-/DCSupplemental.

Published online February 26, 2019.

The IP space is typically less oxygenated compared with the oxygen measured in arterial blood, exhibiting a large variability in partial oxygen pressure (pO_2) within its volume (18–20). In mice, peritoneal pO_2 values vary between 1% and 10% compared with normoxic conditions at 21% (21, 22). In addition to the ambient pO_2 at the implantation site, encapsulated islets are not vascularized and thus rely on the diffusion of oxygen and nutrients from the surrounding environment. It has been hypothesized that the attachment of immune cell populations on the surface of the capsules (manifesting as the onset of fibrotic tissue) acts as a barrier to the influx of oxygen into the interior of the capsules due to the high consumption of oxygen by the immune cells themselves (23, 24). Numerous in vitro studies have shown the effect of limited oxygen supply on encapsulated and nonencapsulated islets (25–28). It has been hypothesized that capsule sizes of no more than a few hundred micrometers are ideal in terms of optimal oxygen supply to the encapsulated islets. Coencapsulation of alginate with materials such as perfluorocarbons (PFCs) (29), prevascularized implants (30), or implants with an additional oxygen supply (31) have been proposed to mitigate hypoxia. A less investigated factor that can affect the exposure of alginate capsules to the ambient oxygen supply is their relative arrangement with respect to each other (32). Whether the capsules are free-floating in the IP space or trapped in tissue, oxygen diffusion across capsule aggregates is governed by principles similar to the ones applicable for oxygen diffusion across a single capsule. A key difference, however, is that although we might assume that the shape of a single capsule stays constant [aside from examples of undesired swelling or degradation (33, 34)], capsule aggregates in the IP space may change size and shape over time.

In vivo quantification of the islet transplant oxygenation within the IP space remains challenging (35). To date, it has not been possible to systematically quantify and spatially resolve oxygen content of alginate capsules in the IP space, in vivo, as well as do so over time. Fluorescence-based, commercially available oxygen microsensors, although easy to use and reliable in measuring oxygen accurately, are invasive and fragile and do not provide a framework for spatially resolved measurements (35). Noninvasive techniques such as imaging have been used to sense oxygen as an alternative to invasive instrumentation: Oxygen-sensitive fluorescent (36), photoacoustic (37, 38), radioactive (39, 40), and magnetic resonance (41) imaging probes have been developed and have demonstrated the ability to quantify oxygen, especially in highly localized structures, such as tumors or immobilized implants. However, in the case of encapsulated islet transplants which are mobile in the IP space, accurate oxygen quantification requires a sensing mechanism that is not depth dependent, does not decay over time thus requiring repeated administration for longitudinal measurements, and does not depend on surrounding tissue to produce a detectable signal.

As an alternative to the above oxygen-sensing approaches, fluorine magnetic resonance imaging (^{19}F-MRI) can be used to noninvasively probe in vivo oxygen content (18, 35, 42–46) (Fig. 1). MRI has long been used in both research and clinical settings to probe anatomy and biological activity with high spatial resolution and without the shortcomings of depth-dependent performance issues and radiation hazards that optical and radionuclide-based imaging methods have, respectively. While in most cases MRI is used to quantify the presence of hydrogen (^{1}H) nuclei, either directly or indirectly through the use of paramagnetic and superparamagnetic contrast agents, other nuclei such as ^{19}F and ^{13}C can also be probed at the appropriate resonance frequency. Fluorine has a resonance frequency close to that of hydrogen and its magnetic resonance signal is not contaminated by any intrinsic fluorine in the body. Due to its high signal-to-noise ratio, fluorine MRI has been used to track cells in vivo (47–49). In addition, fluorine in the form of perfluorocarbons has good solubility for oxygen and has been used to quantify hypoxia in tumors with MRI (42, 50). Previous studies with fluorinated alginate capsules have already demonstrated the feasibility of incorporating MRI labels into alginate and highlight the potential of in vivo imaging in the assessment of cellular therapeutics for diabetes (43–45, 51, 52). A number of

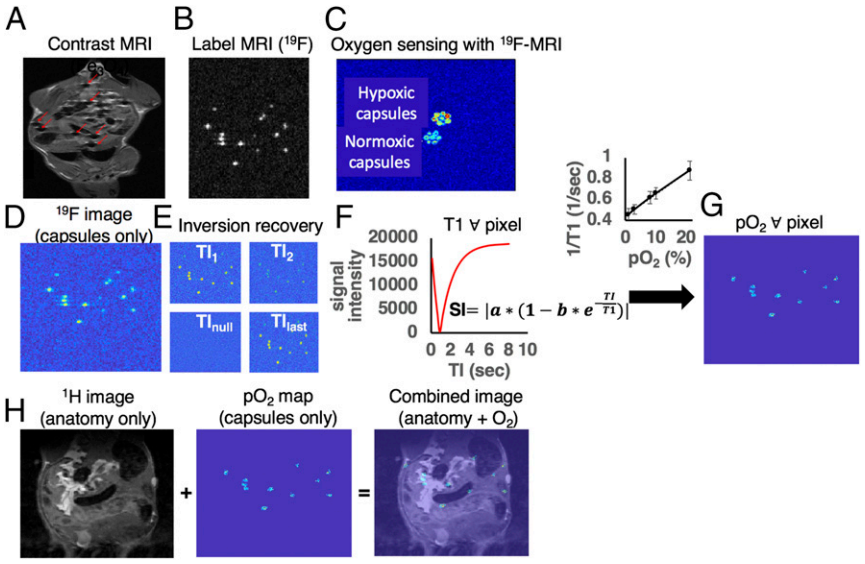

Fig. 1. Noninvasive MRI for simultaneously tracking and determining oxygenation of biomaterial implants. (*A* and *B*) Tracking capsules with contrast-based (Fe_3O_4) vs. label-based (^{19}F) MRI. Alginate capsules loaded with iron oxide nanoparticles appear as local hypointensities ("cold spots," highlighted with red arrows in *A*) in the anatomic background and cannot be easily distinguished from other hypointense structures of the IP space. Alginate capsules loaded with a fluorinated compound appear as hyperintensities ("hot spots" in *B* in null background). (*C*) Fluorine MRI is an imaging technique capable of distinguishing between structures of high and low oxygenation. The image is an MRI-derived oxygen map of two different groups of 1.5-mm diameter fluorinated alginate capsules. The "coldest" group has normal oxygen content and the "hottest" group has had its oxygen displaced by flushing nitrogen gas for several minutes. (*D*–*G*) The imaging flow in measuring oxygen content in alginate capsules using MRI. When the MRI coil is switched to fluorine mode, a scan that visualizes the presence of ^{19}F nuclei can be acquired. (*D*) For PFC-loaded alginate capsules implanted in the IP space of mice, the scan will visualize only the capsules and their relative position. (*E*) To produce oxygen maps with MRI, multiple such scans are acquired while varying for each scan a parameter called inversion time, TI. (*F*) For each pixel in the set of images a plot of pixel intensity vs. TI value is created and the T1 relaxation times are calculated. (*G*) Using calibration curves ($1/T_1$ vs. pO_2, shown above the arrow) we are able to extract the pO_2 value corresponding to each T1 value of each pixel. (*H*) Combining anatomy and pO_2 maps. (*H*, *Left*) When the MRI coil is switched to hydrogen mode, an optional anatomic scan of the animal can be acquired that probes ^{1}H nuclei, thus providing information about the tissue in the IP space. (*H*, *Center* and *Right*) The anatomic scan can be combined with the pO_2 maps previously created (*Center*) to create an overlaid image that shows the capsule pO_2 and their position within the IP space (*Right*). Movie S1 shows a 3D rendering example of a combined anatomy and fluorine MRI image.

studies have also used dual ^{19}F-NMR spectroscopy (21, 53) and ^{19}F-MRI imaging (18, 43, 51) to quantify pO_2 changes in alginate microcapsules implanted in the IP space of mice. However, in all existing studies the pO_2 values were based on averaging the calculated oxygen values over the whole IP volume (21, 43, 51, 53), choosing a single capsule size (21, 51, 53), choosing animal models with fibrotic response that does not align to what is clinically observed (21), and limiting the length or frequency of the study (43, 51).

For image-based, spatiotemporal pO_2 monitoring the large amount of MRI images that need to be collected to track the mobile microcapsules within the volume of the IP space makes manual identification of trends in oxygen a tedious, error-prone task, when pattern identification is based on human visual observation. Of relevance, machine-learning techniques have been widely used to automate tasks in our daily life and, more recently, to facilitate computerized decision making and knowledge acquisition informed by a vast amount of data (54). In the field of biomedical imaging and medical diagnostics, intelligent algorithms are able to review thousands of images and extract high-level information, such as the presence of disease, in an automated way and at a competitive success rate to that of a human observer (55, 56).

In this study our objective was to identify changes in the oxygen content of cellular transplants under the presence of temporal and spatial gradients. To investigate the spatiotemporal dependence of oxygen content in IP-implanted capsules, we analyzed islet-containing as well as empty (no islets present) PFC-loaded 0.5-mm and 1.5-mm diameter alginate microcapsules implanted in the IP space of healthy (implanted with 400 μL of empty capsules) and diabetic (implanted with 400 μL of islet-containing capsules corresponding to 500 islet equivalents) C57BL/6 mice by MRI. The PFC of choice was perfluorocrown ether (PFCE) which has 20 chemically equivalent fluorine atoms, making it an ideal PFC for oxygen studies using MRI (48). We evaluated the fluorinated implants in terms of their stability, fibrotic response, and ability to modulate blood glucose levels in vivo, as well as monitored their insulin production as a function of pO_2 in vitro. We tracked the spatial arrangement of capsules in vivo in the IP space over a period of 3 mo and we quantified their oxygen content as a function of this arrangement. Although fluorine MRI has been used in prior studies to track alginate capsules, this study performs long-term, time and spatially resolved in vivo oxygen tracking of different sized capsules in the IP space, where inherent peristaltic and physical motion can make quantification difficult. To mitigate this challenge, we employed machine learning to efficiently classify the alginate capsules from thousands of 2D images into spatial groups within the IP space and find correlations between their spatial distribution and their oxygen content. We used unsupervised hierarchical clustering to automate the task and facilitate the extraction of associations between oxygen content, time, and spatial arrangement.

Results

The Effect of Fluorine in Fluorinated Alginate Capsules: Stability, Immune Response, and Glycemic Control. Our ability to perform image-based, long-term pO_2 monitoring and simultaneous capsule tracking heavily depends on the long-term stability of the fluorinated capsules and their ability to generate a sustained MRI signal over time. We therefore assessed the possibility for PFCE to leak out of the capsules over time (Fig. 2*A*). To emulate the conditions in the IP space of mice, we kept equal volumes of capsules of each size in retrieved IP fluid mixed with saline and incubated them at 37 °C. The capsules were imaged by MRI at different time points against a standard of known concentration (100% wt/vol PFCE). There was no significant decline of the capsule-to-standard MRI signal ratio, indicating that during the 3-mo course of the in vivo experiments no considerable fluorine signal loss is expected due to leakage. The deviation of the calculated ratio from the expected value of 17% (*SI Appendix*, *Preparation of the PFCE Nanoparticle Emulsion*) is due to signal spillover to neighboring pixels, since the MRI imaging was performed at an axial resolution and an in-plane resolution on the same scale as the size of the capsules.

PFCs are not soluble in water and thus require emulsification before mixing with alginate, although limited studies have been performed using alginate capsules or simple droplets containing pure, nonemulsified PFC (18, 43). The outcome of PFCE emulsification was assessed before and after filtration using dynamic light scattering measurements (*SI Appendix*, Fig. S1*A*). Although the particle size and dispersity are affected by the PFCE concentration in the emulsion (*SI Appendix*, Fig. S1*B*), for the target concentration of 17% vol/vol PFCE we were able to reproducibly fabricate stable nanoparticle emulsions with sizes between 300 nm and 600 nm. The target PFCE concentration was

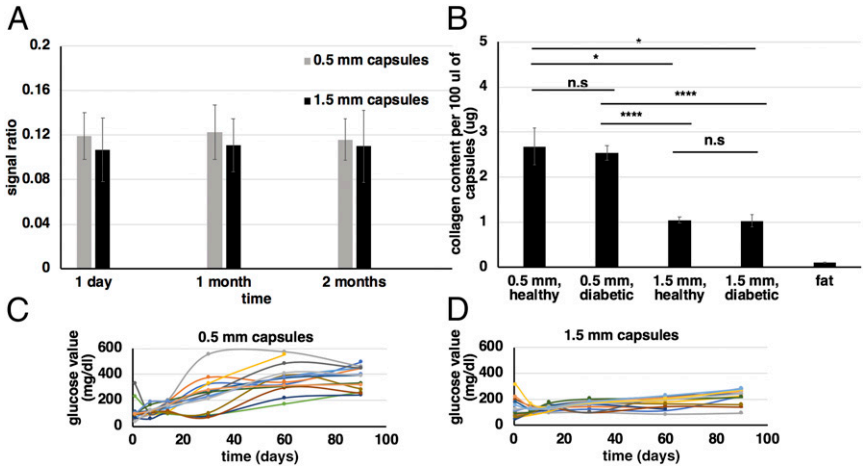

Fig. 2. Alginate fluorocapsules: stability, immune response, and glycemic control. (*A*) Image-based assessment of PFC-loaded capsule stability. For capsules imaged by MRI against a standard of 100% PFCE over a period of 2 mo, there is no considerable loss of MRI signal due to diffusion of PFCE out of the alginate capsules. Capsule-to-standard signal ratio values were calculated by drawing regions of interest (ROIs) on the MRI images of the capsule samples and the standard and calculating the ratio of the average pixel values within these ROIs. The error bars are the propagated SD of the ratio. (*B*) Collagen content per 100 μL of retrieved 0.5-mm and 1.5-mm fluorocapsules after being implanted in the IP space of diabetic (500 islet equivalents per mouse) and healthy (no islets) C57BL/6 mice for over 3 mo (n = 13, 18, 18, 15, or 3 for 0.5-mm capsules in healthy mice, 0.5-mm capsules in diabetic mice, 1.5-mm capsules in healthy mice, 1.5-mm capsules in diabetic mice, and fat samples, respectively). All values are mean ± SEM. (*C* and *D*) In vivo blood glucose values as measured over a period of 3 mo for diabetic STZ-C57BL/6 mice (n = 15 for each implanted capsule size) implanted IP with either 0.5-mm (*C*) or 1.5-mm (*D*) islet-containing fluorocapsules (500 islet equivalents per mouse). The trends observed are comparable to previously published results for nonfluorinated alginate capsules and thus no additional cell toxicity due to PFCE is observed. Experiments were repeated at least twice. For *B* groups were compared with a nonparametric, pairwise Wilcox test with Benjamini and Hochberg (BH) correction for multiple comparisons (*$P < 0.05$; ****$P < 0.0001$; ns, not significant).

chosen as a compromise between making stable emulsions (with small nanoparticle size) and acquiring MRI images with good signal-to-noise ratio (Fig. 2*A*). The fabricated PFCE-loaded alginate capsules are opaque white (*SI Appendix*, Fig. S1*A*, *Inset*).

The fibrotic response of fluorinated capsules was assessed by measuring the collagen content for a fixed volume of capsules (100 μL) which was retrieved from the IP space of mice after a 3-mo implantation period. As is the case with nonfluorinated capsules (11, 13), equal volumes of capsules have significantly higher amounts of collagen in the case of the 0.5-mm capsules compared with the 1.5-mm capsules (Fig. 2*B*, first and second bars vs. third and fourth bars), while there is no significant difference in the fibrotic response between healthy (implanted with empty capsules) and diabetic (implanted with islet-containing capsules) mice for either capsule size (Fig. 2*B*, first bar vs. second bar and third bar vs. fourth bar). For reference, the collagen content from an equal amount of fat tissue is also shown (Fig. 2*B*, fifth bar), from which we can conclude that any contribution of collagen from fat tissue that was accidentally included in the capsule samples during retrieval is negligible. This is particularly relevant to the smaller capsules and their tendency to accumulate to the fatty areas of the IP space.

To study long-term effects of PFCE presence on coencapsulated islets, blood glucose values of diabetic STZ-C57BL/6 mice that were implanted with PFCE-loaded islet-containing transplants (500 islet equivalents per mouse) were monitored over a 3-mo period (Fig. 2 *C* and *D* and *SI Appendix*, Fig. S2 shows average trends). The observed temporal trends, namely the prolonged cure times for 1.5-mm capsules (Fig. 2*D*) and the earlier failure of 0.5-mm capsules (Fig. 2*C*), are consistent with previously published results for non–PFCE-loaded transplants (13) and indicate that the PFCE load has not impeded the ability of islets to secret insulin over a prolonged period of time.

Effects of Varying Partial Pressure of Oxygen on Insulin Secretion of Encapsulated Islets for Fluorinated and Nonfluorinated Alginate Capsules. The effects of low partial pressure of oxygen on encapsulated islets under the absence and presence of PFCE were studied in vitro (Fig. 3). Over a period of 4 d the control (at 21% pO_2) capsules of both sizes (0.5 mm and 1.5 mm in diameter) with or without the PFCE load showed insulin secretion levels consistent with the glucose challenge that the islets were subject to (Fig. 3 *A* and *B*, shaded bars). At a pO_2 of 8–10%, which is similar to the average pO_2 observed within the IP space of mice, secreted insulin levels showed a 30% decrease compared with those at 21% pO_2 for the same glucose stimuli but, in the case of the high-glucose challenge, were still slightly above the threshold of 8 ng/mL necessary for curing diabetes in mice (Fig. 3 *A* and *B*, cross-hatched and solid bars). At a pO_2 of 3%, and with the exception of the 1.5-mm pure (non–PFCE-containing) alginate capsules, a 55–60% decrease in secreted insulin levels was measured, thus falling below this threshold (Fig. 3 *A* and *B*, shaded hatched diagonal bars). For the 1.5-mm pure alginate capsules the percentage of decrease is somewhat smaller around 45%, still resulting in insulin levels below the therapeutic threshold for the lowest oxygen level of 3%. The strong dependence of the ability of islets to secrete insulin on ambient oxygen suggests that when encapsulated islets are implanted in the hypoxic peritoneal cavity, there is a considerable chance that the hypoxic shock will lead to reduced glycemic control. If the capsules are subject to a pO_2 below 8%, for example if the capsules are trapped in areas of the IP space that are more hypoxic than the average value of 8% or if the capsules organize or are fibrosed into large aggregates, the encapsulated islets may not be able to deliver sufficient insulin to properly moderate glucose levels. On the other hand, if the pO_2 in the vicinity of the capsules is maintained at 8% or above, proper glycemic control is possible. This is evident from Fig. 2 *C* and *D*, where blood glucose values can be maintained below the threshold of 220 mg/dL for several months particularly when 1.5-mm capsules are implanted in the IP space (13).

In vitro measurements were initially performed for a time period extending to 12 d to capture the long-term dependence of insulin secretion on pO_2 (Fig. 3 *C* and *D*). However, the measurements for the last time point (day 12) showed that there was reduced insulin secretion not attributed to reduced pO_2 that is observed in both the control (Fig. 3*D*, normoxic) and the test (Fig. 3*C*, hypoxic) samples. We attribute the reduced insulin secretion by the control samples to islet death that occurs in nonimplanted, encapsulated islets when they stay in cell culture for a prolonged period of time of a few weeks (57). While detailed theoretical and experimental studies (25, 29) have confirmed the enhanced oxygen permeability of alginate when mixed with PFCs, ultimately, no significant difference in the insulin secretion results was observed between pure alginate and PFCE alginate capsules.

In Vivo Variability of the Oxygen Environment of Encapsulated, Transplanted Islets. To understand what oxygen conditions the encapsulated islets encounter in vivo, MRI measurements were conducted following implantation of fluorocapsules of two different sizes (0.5 mm and 1.5 mm diameter) into the IP space of

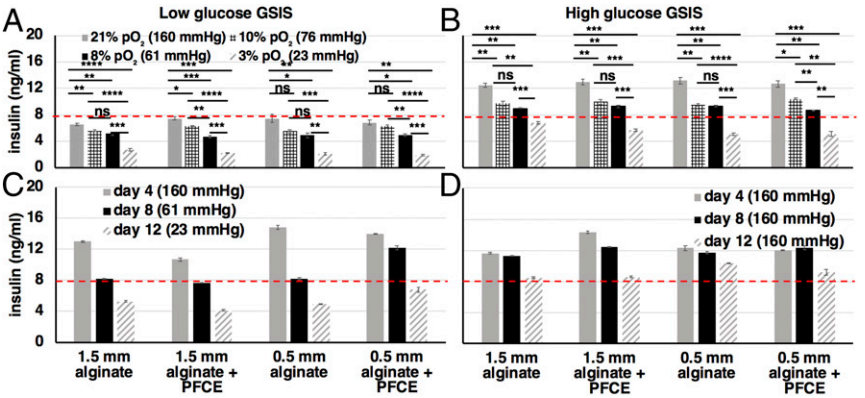

Fig. 3. Dependence of encapsulated islet functionality on oxygen conditions. (*A* and *B*) In vitro low (*A*, 2 mM) and high (*B*, 20 mM) glucose-stimulated insulin secretion assay (GSIS) of encapsulated islets (500 islet equivalents per group) under different oxygen conditions (21%, shaded bars; 10%, cross-hatched bars; 8%, solid bars; 3%, shaded hatched diagonal bars). From the high-glucose GSIS assay it is evident that at 3% pO_2 (shaded hatched diagonal bars) the amount of secreted insulin is below the threshold of 8 ng/mL (red dashed line) necessary for curing diabetes in adult mice when implanted with 500 islet equivalents. At 8–10% pO_2 (solid and cross-hatched bars), which is within the average range of oxygen pressure in the IP space of mice, the amount of secreted insulin is borderline above the therapeutic threshold. Measurements were performed daily over a period of 4 d. (*C* and *D*) High-glucose GSIS data over a 12-d period where the pO_2 is changed every 4 d (*C*) and is maintained at 21% for the full 12-d period (*D*). Even under normoxic conditions (*D*) islet functionality deteriorates over time. For all graphs values are mean ± SEM. All experiments were repeated at least twice. Groups were compared with a nonparametric, pairwise Wilcox test with Benjamini and Hochberg (BH) correction for multiple comparisons (*$P < 0.05$; **$P < 0.01$; ***$P < 0.001$; ****$P < 0.0001$; ns, not significant).

healthy (implanted with empty capsules) and diabetic (implanted with islet-containing capsules) mice ($n = 5$ for each capsule size), with oxygen maps regularly produced over a period of 3 mo (at 1 d, 7 d, 14 d, 30 d, 60 d, and 90 d postimplantation) (Fig. 4). Quantified oxygen content results showed significant variability both from one mouse to another and within different regions of the IP space of a single animal, in agreement with previous reports (43). The median of the pO_2 distribution is below 10% (75 mmHg) (Fig. 4*A*) as expected from previous studies (22, 43, 58) and in accordance with in vivo measurements in the IP space of mice using an optical-based oxygen microsensor (*SI Appendix*, Fig. S4).

Negative pO_2 values have been attributed by previous groups to the difference between ex vivo (calibration studies) and in vivo (animal studies) ambient conditions (18). As a result of the ex vivo studies (*SI Appendix*, *Fluorine MRI and Oxygen Calibration Measurement*), calibration curves (Fig. 4*B*) map the calculated relaxation rates R1 (1/s) to oxygen pressure values (mmHg and/or $\%pO_2$). The reliability of these curves can affect how accurately MRI data are mapped and meaningfully converted to real oxygen values. To produce these calibration curves images of the calibration samples are taken at different inversion times (TI) (Fig. 1 and *SI Appendix*, *Fluorine MRI and Oxygen Calibration Measurement*). Representative graphs ("TI graphs") of the dependence of pixel intensity on TI and their corresponding fits ("TI fits"; *SI Appendix*, Eq. **S1**) are shown for both ex vivo calibration experiments (Fig. 4*C*, *Top* row) and in vivo studies (Fig. 4*C*, *Bottom* row). Due to the limited number of TIs imposed by the need to minimize scanning time, the TI graphs may not always capture the full extent of the theoretical curve described in *SI Appendix*, Eq. **S1**. In addition, occasional poor signal-to-noise ratio and movement, especially in the case of the in vivo studies, can hinder the accuracy of the TI fits.

High pO_2 values above 21% are the result of suboptimal TI fits (Fig. 4*C*, *Bottom* row) on noisy TI curves, leading to the large variability in the calculated average pO_2 values (Fig. 4*A*). Noise on the in vivo TI curves (Fig. 4*C*, *Bottom* row) that is not observed on the ex vivo TI curves (Fig. 4*C*, *Top* row) is due to the fact that the capsules in vivo are free-floating in the IP space and subjected to movement over time due to peristaltic motion. Movement due to respiration might also be a complicating factor; however, such effects were mitigated by maintaining a slow and constant breathing rate below 20 respirations per minute during each imaging experiment by controlled anesthesia. Movement by either reason inevitably exposes the capsules to the highly variable oxygen environment of the IP space (22, 43). In addition, capsule movement reduces the possibility of them maintaining constant presence around—or exposure to—well vascularized and oxygenated areas. The estimated error in the calculated pO_2 values due to the limited number of TIs and the accuracy of TI fits on noisy TI graphs was 10% of the average value.

Over prolonged periods of time, there is a tendency for 0.5-mm capsules to combine in larger aggregates that are commonly trapped in the fatty areas (i.e., mesentery and epididymal fat pads) of the lower extremities of the animals (Fig. 5*A*, *Right*, *Top* five panels), while this tendency is less pronounced for 1.5-mm capsules (Fig. 5*B*, *Right*, *Top* five panels). Although we have observed variations in capsule volumetric distribution as a result of the surgery conditions (e.g., slight difference in the incision position or implantation technique), typically the first day after implantation the capsules of either size appear more dispersed within the IP space compared with later time points (Fig. 5 *A* and *B*, *Left*, *Top* five panels). Calculated pO_2 spatial maps over the same time points indicate that large capsule dispersity results in large variability in pO_2 values (Fig. 5*A*, *Left*, *Middle* five panels and Fig. 5 *B*, *Left* and *Right*, *Middle* five panels), while as the dispersity becomes smaller over time, the pO_2 values appear lower and more uniform (Fig. 5*A*, *Right*, *Middle* five panels). A further quantitative verification of this observation is shown in Table 1, where the percentage of difference of pO_2 over a period of 90 d (ΔpO_2) is compared side by side with the percentage of difference, over the same time period, in the median interquartile range (Δiqr) of each pixel's position in the MRI image that corresponds to capsule signal (*SI Appendix*, *Data Visualization, Capsule Clustering, and Statistical Analysis* and Eq. **S2**). In the case of 0.5-mm implanted capsules, almost all mice show a decrease in pO_2 with a corresponding decrease in median iqr. In the case of the 1.5-mm implanted capsules, the majority of mice exhibit a variable iqr with no obvious decrease in pO_2.

The change of capsule dispersity over time results in the arrangement of capsules in spatial "clusters" whose size (referred

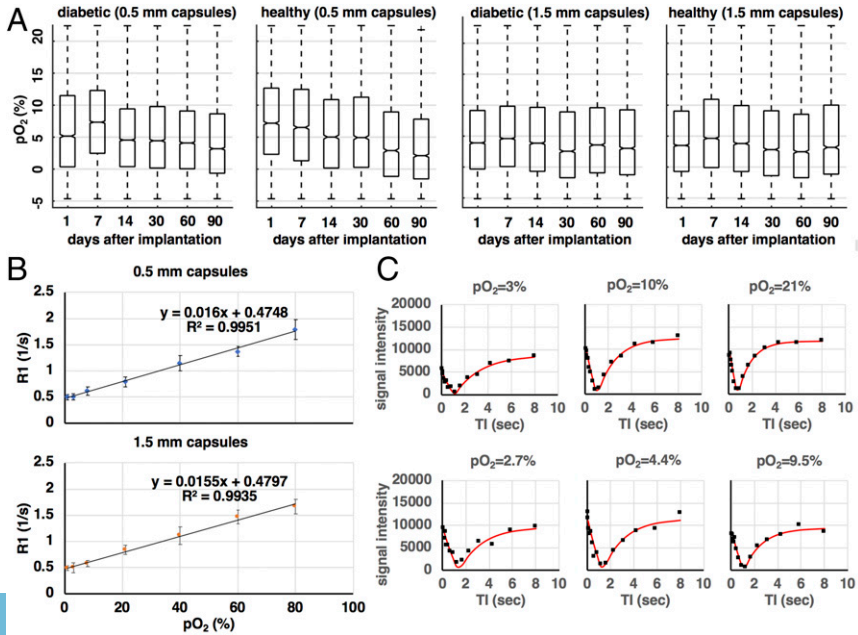

Fig. 4. Measuring pO_2 distribution of encapsulated islets implanted in the IP space of mice. (*A*) Calculated pO_2 distributions for all four groups of mice ($n = 5$ for each group, healthy mice have no islets implanted, diabetic mice have 500 islet equivalents implanted per mouse) as a function of time postimplantation. The median of the distribution for all animal groups is below 10% (75 mmHg) consistent with typical pO_2 values in the IP space. A declining trend is observed for the healthy mouse group with 0.5-mm capsules. Outliers that fall above the normoxic level of 21% are attributed to suboptimal TI fits. Negative outliers are attributed to the different imaging conditions ex vivo and in vivo. (*B*) Calibration curves for samples of 0.5-mm and 1.5-mm capsules in a vial. Values are mean ± SD of all pixel values defined by a circular ROI on the acquired MRI images. (*C*, *Top*) TI curves (black points) and TI fits (red line) for a calibration sample containing 0.5-mm capsules in a vial and for three different pO_2 values: 3% (*Left*), 10% (*Center*), and 21% (*Right*). (*C*, *Bottom*) TI curves (black points) and TI fits (red line) for 0.5-mm capsules implanted in the IP space of mice for three different pO_2 values: 2.7% (*Left*), 4.4% (*Center*), and 9.5% (*Right*). In vivo the TI fits have a larger deviation from the measured data due to motion (peristaltic, respiratory) occurring during the MRI measurement. Each MRI measurement is the average of two acquisitions.

to henceforth as "occupancy," indicating the number of image pixels belonging to a specific cluster) and number also varies with time (Fig. 5 *A* and *B*, *Bottom* and Fig. 5 *C* and *D*). To classify each image pixel that corresponds to the real fluorine signal to an identified cluster, we employed an unsupervised machine-learning algorithm (hierarchical clustering) that is able to automatically browse through thousands of 2D MRI images and identify such clusters and calculate their occupancy, their number, and their position (*SI Appendix*, *Data Visualization, Capsule Clustering, and Statistical Analysis*). Using silhouette scores as well as visual inspection on randomly sampled images (*SI Appendix*, Eq. **S3**) we were able to assess the quality of clustering assignments of each image pixel as satisfactory (*SI Appendix*, Fig. S5).

Image Clustering Allows for More Accurate Identification of pO_2 Gradients Within Capsule Aggregates. A quantitative estimation of the oxygen content in implanted fluorocapsules was performed, and its correlation to their spatial and temporal distribution for both capsule sizes was determined (Fig. 6). Due to the large variability in oxygen partial pressure in the IP space (22, 43), it is difficult to identify trends in the dependence of fluorocapsule oxygen content as a function of time based on average or median oxygen values alone (Fig. 4*A*). Instead, we estimated the percentage of image pixels for every animal of each group (and over all image slices with true fluorine signal) with a pO_2 value below 8% (Fig. 6A, *Top*) for clusters of all possible occupancies, as well as the number of identified clusters as a function of time (Fig. 6*A*, *Bottom*) for each of the four animal groups. Over a period of 3 mo data show that there is a larger variability on the above metrics for both healthy (without islets) and diabetic (with islets) animals with 0.5-mm implanted capsules (Fig. 6*A*, *Top* and *Bottom Left*). In the case of mice implanted with 1.5-mm implanted capsules, the variability was less pronounced (Fig. 6*A*, *Top* and *Bottom Right*). Between days 7 and 14 post-implantation, inflections in oxygen trends were observed in both the number of clusters and the percentage of pixels with pO_2 smaller than 8% for all animal groups (Fig. 6*A*). This observation may be the result of increased accumulation of immune cells in response to implanted alginate capsules within the same period, as has been verified in a previous study (11).

We subsequently looked at cluster occupancy, which is also indicative of the cluster size, as an additional feature that may relate to the capsule oxygen content (Fig. 6*B*). Oxygen content

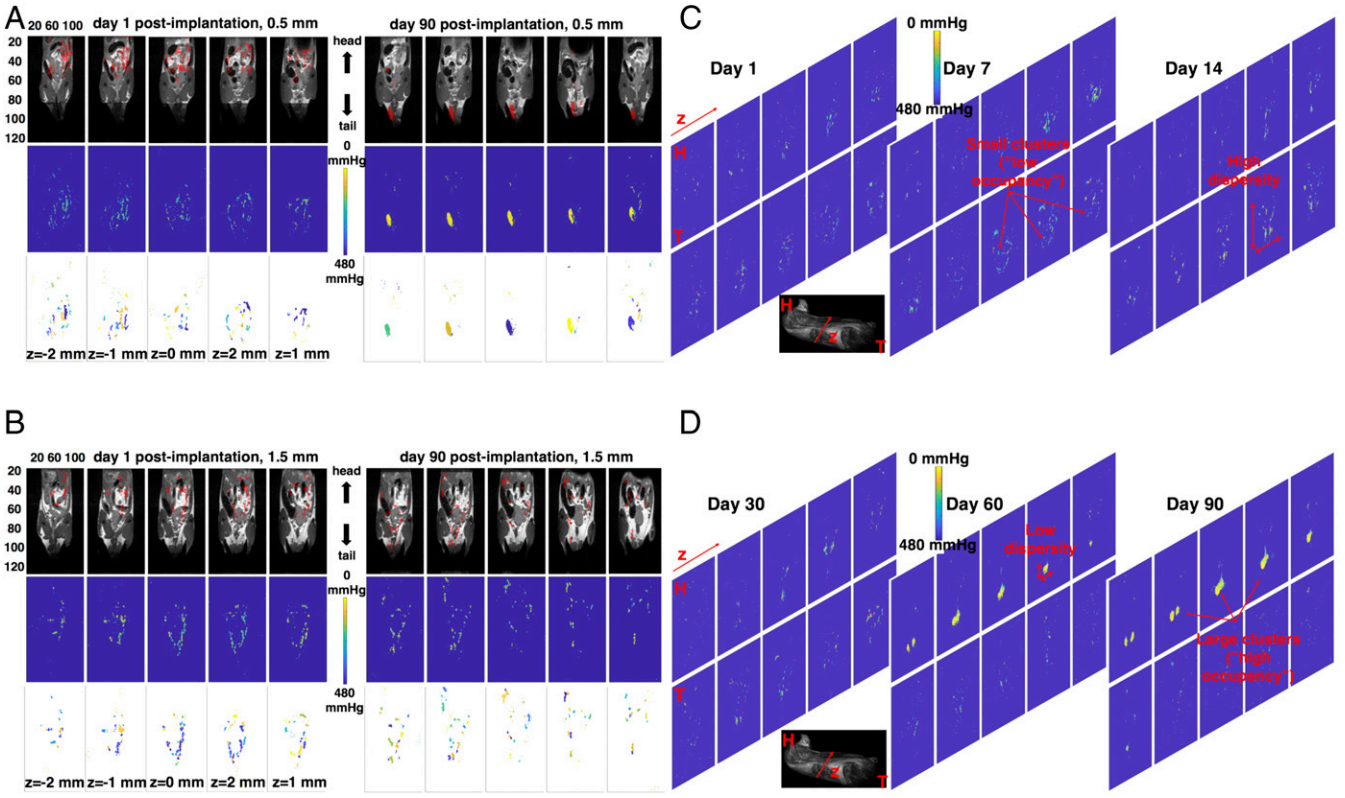

Fig. 5. Spatiotemporal in vivo pO_2 tracking and clustering. (*A*, *Top*) In vivo slice-by-slice fused MRI images of fluorocapsule distribution (^{19}F-MRI, red) and soft tissue anatomy (^{1}H-MRI, grayscale) at day 1 (*Left*) and day 90 (*Right*) postimplantation for 0.5-mm fluorocapsules implanted in a healthy mouse (no islets, empty capsules). *z* denotes depth within the mouse body. Each panel corresponds to a different coronal slice along *z*. The capsules of this size tend to aggregate in large clusters over time. (*B*, *Top*) In vivo slice-by-slice fused MRI images of fluorocapsule distribution (^{19}F-MRI, red) and soft tissue anatomy (^{1}H-MRI, grayscale) at day 1 (*Left*) and day 90 (*Right*) postimplantation for 1.5-mm fluorocapsules implanted in a healthy mouse (no islets, empty capsules). The capsules of this size maintain a broad and rather disperse distribution throughout the 90-d time window. The images for each capsule size correspond to a single mouse with the most extreme manifestation of tight (*A*) and broad (*B*) spatial distribution. The five most central 2D slices are shown in each case. (*A* and *B*, *Middle*) Calculated pO_2 spatial color maps using the procedure outlined in Fig. 1. Large capsule aggregates (*A*, *Right*, *Middle*) demonstrated the lowest pO_2 levels (brighter colors correspond to decreased pO_2). (*A* and *B*, *Bottom*) Using hierarchical clustering capsule aggregates can be labeled into clusters. Each cluster in the images corresponds to a different color. (*C* and *D*) Temporal evolution of capsule organization and oxygen content for a mouse with 0.5-mm, empty (no islets) implanted capsules. The 10 most central coronal slices are shown. Examples of large and small clusters of low and high dispersity are highlighted with red arrows. The bottom grayscale image is an MRI anatomical image of the mouse (MRI operating in hydrogen mode) that shows the position of the slices along the *z* plane (anterior–posterior view) and with respect to the head (H) and tail (T) of the mouse. Each MRI measurement is the average of two acquisitions. Movie S1 shows a 3D rendering example of a combined anatomy and fluorine MRI image.

Table 1. Percentage of change in pO_2 and iqr over a period of 90 d

Mice	% Δ(pO_2)	% Δ(iqr)
0.5-mm capsules		
Healthy mice		
Mouse 1	−15.8	51.2
Mouse 2	−28.2	−26.7
Mouse 3	−26.5	−29.8
Mouse 4	−42.0	−40.8
Mouse 5	−34.4	−26.3
Diabetic mice		
Mouse 1	−4.7	30.6
Mouse 2	−14.7	−38.1
Mouse 3	−15.7	−47.3
Mouse 4	−19.2	−52.1
Mouse 5	−22.6	−48.9
1.5-mm capsules		
Healthy mice		
Mouse 1	−2.5	187.1
Mouse 2	12.3	27.4
Mouse 3	−14.1	−21.3
Mouse 4	9.4	6.2
Mouse 5	−0.6	−29.2
Diabetic mice		
Mouse 1	−1.2	156.2
Mouse 2	6.5	5.1
Mouse 3	0.4	10.2
Mouse 4	−0.9	−13.1
Mouse 5	0.4	29.9

Each row corresponds to an individual mouse from each of the four groups studied. For 0.5-mm capsules, decrease in pO_2 over time is accompanied by decrease in capsule dispersity for both islet-containing (diabetic mice) and empty (healthy mice) capsules, with the exception of one healthy mouse. For 1.5-mm capsules, no consistent trend across each animal group can be observed. pO_2 and iqr values are calculated over 12 image slices for each mouse. Each MRI measurement is the average of two acquisitions.

(represented as a percentage of image pixels with pO_2 below a given value) as a function of time was determined for clusters with two different occupancy ranges. We chose a middle boundary occupancy condition of 20 pixels, which corresponds to a maximum dimension of 7.8 mm, and a minimum occupancy of 3 pixels, which corresponds to a maximum dimension of 1.2 mm. The minimum occupancy was chosen as it is an intermediate value between the two different capsule diameters investigated in this study and is used to minimize bias from image noise and suboptimal TI fits. For all animal groups, clusters with occupancy above the boundary of 20 pixels (Fig. 6*B*, *Top*, gray bars) had significantly lower oxygen values (higher percentage of image pixels with pO_2 less than 8%) compared with clusters with occupancy below the boundary (Fig. 6*B*, *Top*, black bars). As expected, in the case of all animal groups implanted with 0.5-mm capsules (Fig. 6*B*, *Top*, first and second panels), the percentage of pixels with higher oxygenation is initially higher compared with the animal groups with implanted 1.5-mm capsules (Fig. 6*B*, *Top*, third and fourth panels), which is justified by their smaller diameter. Over time, however, a larger percentage of pixels for the smaller 0.5-mm capsules became less oxygenated (Fig. 6*B*, *Top*, first and second panels), which was not the case in the animal groups with implanted 1.5-mm capsules, where the variation of oxygen content is not significant (Fig. 6*B*, *Top*, third and fourth panels). This indicates that although at the end of the study (90 d postimplantation) the average levels of oxygenation were not significantly different between 0.5-mm and 1.5-mm capsules, higher temporal gradients of pO_2 were observed for 0.5-mm capsules when they were arranged in clusters of higher occupancy (Fig. 6*B*, *Top*, first and second panels, gray bars).

The average number of clusters below and above the boundary value of 20 pixels was identified in each animal group (Fig. 6*B*, *Bottom*). Overall, there was a larger number of clusters within the smaller-occupancy range (Fig. 6*B*, *Bottom*, black bars) compared with clusters within the higher-occupancy range (Fig. 6*B*, *Bottom*, gray bars) throughout the duration of the study for all animal groups. The number of clusters in either occupancy range does not vary significantly across all animal groups. For the group of diabetic mice with implanted 0.5-mm capsules (islet-containing, 500 islet equivalents per mouse) the number of clusters within the smaller-occupancy range decreases significantly compared with the other groups (Fig. 6*B*, *Bottom*, first panel, black bars); however, the number of capsules within the larger-occupancy range does not follow a proportional increase (Fig. 6*B*, *Bottom*, first panel, gray bars), which indicates that the latter clusters may increase over time in size as opposed to number. For the group of healthy mice with implanted 0.5-mm capsules (blank capsules, no islets) there is no significant decrease in the number of clusters within the small-occupancy range, while there is a noticeable but nonsignificant decrease in the number of clusters within the large-occupancy range (Fig. 6*B*, *Bottom*, second panel). This particular group has the smallest number of high-occupancy clusters at day 90 compared with all of the other groups, but also the largest-sized clusters (Fig. 6*C*, *Bottom Left*). Both healthy (without transplanted islets) and diabetic (with transplanted islets) mice with implanted 0.5-mm capsules demonstrate the most significant changes in pO_2 over time as well as between clusters of different occupancies (Fig. 6*B*, *Top* and *Bottom*, first and second panels).

We also studied the correlation between average pO_2 per cluster and cluster occupancy for days 1 and 90 postimplantation (Fig. 6*C*). The variability in average pO_2 is larger for clusters of small occupancy. The most significant contributing factor to this variability is the larger range of movement in small clusters compared with larger ones, which also results in higher rates of underfitting of the TI plots. Above the occupancy threshold of 20 pixels (Fig. 6*C*, red dashed line in all panels) the variability decreases to levels that are anticipated in the IP space. Notably, the distribution of 0.5-mm capsules exhibits larger "tails" of high-occupancy, low-pO_2 clusters (Fig. 6*C*, *Top* and *Bottom Left*). This effect is more pronounced for the case of 0.5-mm capsules implanted in healthy mice (Fig. 6*C*, *Bottom Left*).

Discussion

In this study, we developed an image-based analytical framework appropriate for tracking unconstrained cellular implants and their physiological conditions over time in implantation sites that can hold a large curative transplant biomass, thus allowing for significant transient effects within the implant. As an example, we investigated in vivo the temporal and spatial dependence of the oxygen content available to encapsulated islets within two different capsule sizes, implanted in the IP space of C57BL/6 mice using fluorine MRI and clustering algorithms. In vitro results show that at a pO_2 of 8–10% islets encapsulated within capsules of either size, with or without PFCE, can borderline sustain an insulin secretion level slightly above 8 ng/mL, minimally needed to maintain normoglycemia in adult mice when they are implanted with a total of 500 islet equivalents per mouse (Fig. 3). However, at a pO_2 of 3% the insulin secretion levels fell significantly below that threshold. In vivo, image-based calculation of capsule spatial dispersity correlates with oxygen content and shows that as the capsules become less dispersed within the IP cavity their oxygen levels decrease (Fig. 5 and Table 1). This trend was true for 0.5-mm implanted capsules over a period of 90 d (Table 1, top 10 rows); however, no particular trend was

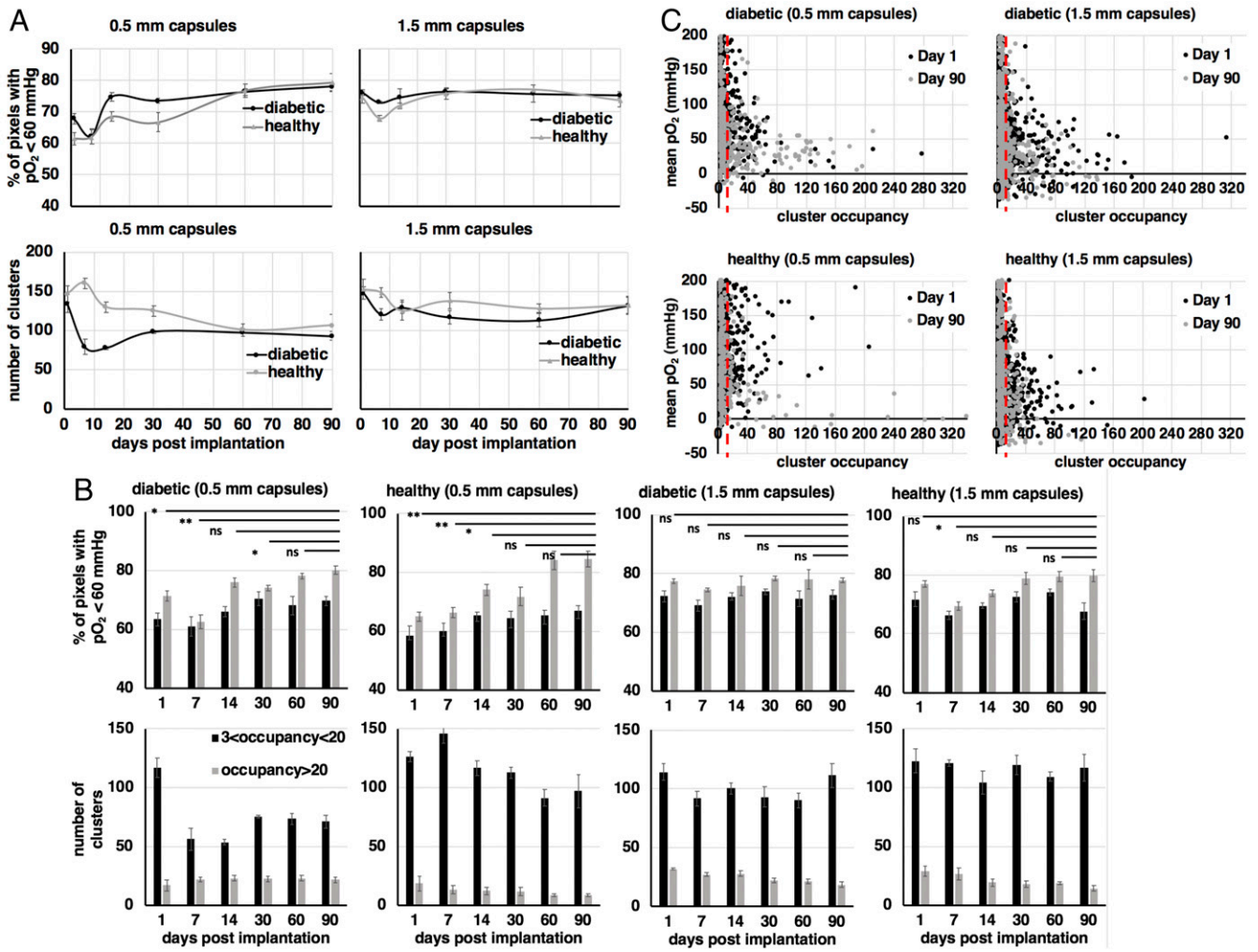

Fig. 6. Quantitative pO_2 spatiotemporal tracking using unsupervised cluster analysis. (*A*) Percentage of pixels with pO_2 values less than 60 mmHg (*Top*) and total number of identified clusters (*Bottom*) over time for each of the four animal groups. These metrics appear to fluctuate from a smooth trend between days 7 and 14, similar to the temporal dependence of the immune cell populations attached to alginate, as shown in previous studies. When clusters are stratified to high (more than 20 pixels) and low (less than 20 pixels) occupancy, statistically significant differences are observed in the oxygen content of the implants particularly for the high-occupancy clusters and for 0.5-mm capsules (*B*, *Top*, first and second panels, gray bars). Throughout the duration of the study low-occupancy clusters are significantly larger in number compared with the high-occupancy ones for all animal groups. (*C*) Scatter plots of mean pO_2 per cluster vs. cluster occupancy for animal groups with 0.5-mm implanted capsules (*Left*) and 1.5-mm capsules (*Right*) for days 1 (black circles) and 90 (gray circles) postimplantation. For all graphs values are mean ± SEM. Groups were compared with a parametric, pairwise Student's *t* test, with variance relaxation and Benjamini and Hochberg (BH) correction for multiple comparisons (*$P < 0.05$; **$P < 0.01$; ns, not significant). Each MRI measurement is the average of two acquisitions.

observed in dispersity and oxygen levels for 1.5-mm implanted capsules (Table 1, bottom 10 rows).

The assignment of image pixels into clusters allowed us to further derive significant associations between the oxygen content and the spatial arrangement of implanted capsules that otherwise could not be observed if we average calculated pO_2 values over the total image signal. Longitudinal measurements were performed to determine these associations over time. We found that 0.5-mm capsules tend to organize in clusters of higher occupancy (larger size), consistent with their tendency to become less disperse over time (Fig. 5). Furthermore, clusters of larger size exhibit a decrease in measured oxygen levels as opposed to individual capsules or small clusters that maintain their oxygen content over time (Fig. 6).

Although our work does show not only the intracapsular oxygen values, especially in the case of the small 0.5-mm capsules, the tendency for aggregation in clusters makes a measurement of the cluster oxygenation (as opposed to the individual capsule oxygenation) more meaningful. To achieve sufficient resolution and signal-to-noise ratio in the MRI images to quantify oxygen content across single capsules scan time would need to be substantially increased. Measurement of intracapsular partial oxygen pressure by inserting the oxygen optical microsensor into the capsule was unsuccessful and resulted in damage of the sensor. The observation that no significant difference in insulin secretion was measured between fluorinated and nonfluorinated capsules (Fig. 3) suggests that the increased solubility of oxygen in perfluorocarbons does not result in a functionally significant pO_2 gradient between the capsule interior (where the islets are located) and the surrounding IP environment.

The findings in this study can be used to guide more efficient designs of the bioartificial pancreas in terms of its optimal implant size, cell quantity, and distribution within the implantation site. For example, if the smaller-sized capsules have initially higher levels of oxygenation that decreases over time due to the formation of large clusters, as shown here, it might be beneficial to develop scaffolds

that will host small-sized capsules at well-defined, equidistant positions within the implantation site. The relationship between the total curative implanted biomass and the available oxygen supply at the implantation site is another question that our methodology is well suited to address. Furthermore, the methodology presented here could be expanded to larger bipedal animals, such as nonhuman primates, where capsule aggregation at the lower extremities due to gravitational pull is more pronounced and is anticipated to lead to higher variability in measured oxygen content.

Despite nonoptimal experimental factors, such as the trade-off between animal throughput and ideal MRI settings, capsule motion during each measurement, and deviation between the conditions of ex vivo oxygen calibration and in vivo measurements, we were able to observe significant trends in the spatial arrangement and oxygen content of implanted encapsulated islets over time. The use of machine learning significantly enhanced our ability to perform image-based assessment of oxygenation in cellular implants in vivo over a large volume and could be expanded to the study of other facets of implant function such as immunogenicity, angiogenic response, viability, and therapeutic efficiency. Beyond unsupervised clustering algorithms, deep-learning algorithms offer a promising avenue for delineating important correlations within the multiparametric implant environment by using as input a combination of data such as imaging, chemical, or biological sensor data. The insight gained from such an approach may help engineer improved implant designs that lead to prolonged cure windows.

Aside from therapeutic cellular encapsulation systems in biomaterials, the interrogation of oxygen conditions and how they affect transient cell populations such as immune cells, systemically administered therapeutic cell grafts, and metastatic cancer cells, but also noncellular drug delivery systems and biosensors, has been primarily limited to in vitro studies due to the lack of whole-body in vivo imaging techniques that are able to perform sensitive measurements over a large volume. Fluorine MRI has the ability to do so with a sensitivity that can be tuned by the magnetic-field strength, as well as simultaneously probe the oxygen microenvironment through the collection of a vast amount of 3D data. As shown in the paradigm of this study, the drawback of tedious data collection can be mitigated by advanced analytics based on machine learning that facilitates the derivation of patterns from a large number of images.

Finally, the clinical relevance of fluorine MRI tracking of cell populations is currently being demonstrated (59, 60). This image-based technique may thus allow the tracking and physiological monitoring of disease as well as novel therapies noninvasively in humans.

Materials and Methods

Detailed description of materials and methods can be found in *SI Appendix*.

Preparation of the PFCE Nanoparticle Emulsion. We created PFCE–lipid nanoparticle emulsions by mixing and sonicating a PFCE, ethanol, 1,2-Dioleoyl-sn-glycero-3-phosphocholine, and deionized water mixture.

PFCE Loaded Alginate Solution and Islet Microencapsulation. Rat islets were isolated and mixed with alginate at a concentration of 500 islet equivalents per 0.4 mL of alginate. Capsules were formed from the islet–alginate mixture and, before being implanted into mice, they were washed with sterile saline.

Toxicity Study and Leakage Study. Islet-containing PFCE-loaded alginate capsules were implanted through laparotomy in the IP space of diabetic mice and their blood glucose levels were monitored through sequential blood draws. PFCE capsules of two different sizes were prepared as described above. At different time intervals the capsules were imaged using fluorine MRI against a standard sample containing 100% PFCE.

In Vitro Hypoxia Experiment—Glucose-Stimulated Insulin Secretion Assay. The effect of three different hypoxic conditions on islet survival has been assessed in vitro. Each day an islet glucose-stimulated insulin secretion (GSIS) assay was performed in a subset of islet-containing alginate capsules incubated under different hypoxic conditions, and the insulin secreted by the islets in response to a glucose stimulus was measured. The same experiment was performed for pure alginate, islet-containing capsules that were not loaded with PFCE.

Fluorine MRI and Oxygen Calibration Measurement. MRI imaging was performed using a 7-T Varian 7T/310/ASR-whole mouse MRI system. A dual-mode ($^{1}H/^{19}F$) volume coil was used for all of the imaging studies. For each capsule size, five different samples were created, with each sample being continuously flushed for at least 2 h with balanced nitrogen gases of a different O_2 concentration. The samples were subsequently imaged with MRI in fluorine mode and their T1 values were calculated.

In Vivo Hypoxia Experiment—MRI Imaging. All animal experiments were performed in accordance with detailed Institutional Animal Care and Use Committee protocols as reviewed and approved by the Committee on Animal Care of the Massachusetts Institute of Technology. Ten diabetic and 10 healthy adult C57BL/6 mice were used in the in vivo experiments. Diabetic mice were implanted with islet-containing capsules as described above, while healthy mice were implanted with equal volumes (400 μL per mouse) of empty capsules (no islets). Each group of mice was imaged with MRI in fluorine mode at different days during a 90-d period.

In Vivo Hypoxia Experiment—Optical Oxygen Microsensor. The sensor was placed at five different locations in the IP space of mice in the supine position. Using ultrasound guidance, we inserted the oxygen microsensor 5 mm deep into the IP space and recorded pO_2 measurements after the sensor readings were stabilized at each location in the IP cavity.

Blood Glucose Monitoring. Blood glucose levels for all diabetic mice studied were estimated using a commercially available, handheld glucometer. Before any treatment the glucose levels of diabetic mice were confirmed to be consistently high for ~2 wk.

Fibrosis Quantification at Terminal Time Point (ex Vivo). Capsules were retrieved from euthanized mice 3 mo after implantation. A hydroxyproline assay kit was used to prepare the samples in each well for quantification.

Data Visualization, Capsule Clustering, and Statistical Analysis. All MRI images were acquired using the Vnmrj software and were visualized using MATLAB. The T1 maps were calculated using Julia. Statistical analysis was performed using RStudio.

ACKNOWLEDGMENTS. All animal imaging studies were performed at the Animal Imaging and Preclinical Testing (AIPT) core at the Swanson Biotechnology Center of the Koch Institute for Integrative Cancer Research at Massachusetts Institute of Technology (MIT). The authors thank Prof. Nicolas Bertrand from Quebec University for his assistance with the development of the PFCE emulsion protocol, Dr. Scott Malstrom from AIPT at MIT for his assistance with MRI instrumentation and initial measurements, and Prof. Alan Jasanoff from MIT for the useful discussions on fluorine MRI imaging. This work has been supported by the Juvenile Diabetes Research Foundation (JDRF) (Grant 17-2007-1063), by the Leona M. and Harry B. Helmsley Charitable Trust Foundation (Grants 09PG-T1D027 and 2017PG-T1D027), by the Parviz Tayebati Research Fund, and in part by the Koch Institute Support (core) Grant P30-CA14051 from the National Cancer Institute. J.C.D. was supported by a JDRF postdoctoral fellowship (Grant 3-PDF-2015-91-A-N).

1. Rankin EB, Giaccia AJ (2016) Hypoxic control of metastasis. *Science* 352:175–180.
2. Taylor CT, Colgan SP (2017) Regulation of immunity and inflammation by hypoxia in immunological niches. *Nat Rev Immunol* 17:774–785.
3. Malda J, Klein TJ, Upton Z (2007) The roles of hypoxia in the *in vitro* engineering of tissues. *Tissue Eng* 13:2153–2162.
4. Nobre AR, Entenberg D, Wang Y, Condeelis J, Aguirre-Ghiso JA (2018) The different routes to metastasis via hypoxia-regulated programs. *Trends Cell Biol* 28:941–956.
5. Appel AA, Anastasio MA, Larson JC, Brey EM (2013) Imaging challenges in biomaterials and tissue engineering. *Biomaterials* 34:6615–6630.
6. Di Corato R, et al. (2013) High-resolution cellular MRI: Gadolinium and iron oxide nanoparticles for in-depth dual-cell imaging of engineered tissue constructs. *ACS Nano* 7:7500–7512.
7. Berdichevski A, Simaan Yameen H, Dafni H, Neeman M, Seliktar D (2015) Using bimodal MRI/fluorescence imaging to identify host angiogenic response to implants. *Proc Natl Acad Sci USA* 112:5147–5152.
8. Lim F, Sun AM (1980) Microencapsulated islets as bioartificial endocrine pancreas. *Science* 210:908–910.
9. Desai T, Shea LD (2017) Advances in islet encapsulation technologies. *Nat Rev Drug Discov* 16:338–350.

10. Strand BL, Coron AE, Skjak-Braek G (2017) Current and future perspectives on alginate encapsulated pancreatic islet. *Stem Cells Transl Med* 6:1053–1058.
11. Doloff JC, et al. (2017) Colony stimulating factor-1 receptor is a central component of the foreign body response to biomaterial implants in rodents and non-human primates. *Nat Mater* 16:671–680.
12. Vegas AJ, et al. (2016) Combinatorial hydrogel library enables identification of materials that mitigate the foreign body response in primates. *Nat Biotechnol* 34: 345–352.
13. Veiseh O, et al. (2015) Size- and shape-dependent foreign body immune response to materials implanted in rodents and non-human primates. *Nat Mater* 14:643–651.
14. Vegas AJ, et al. (2016) Long-term glycemic control using polymer-encapsulated human stem cell-derived beta cells in immune-competent mice. *Nat Med* 22:306–311.
15. de Vos P, Hamel AF, Tatarkiewicz K (2002) Considerations for successful transplantation of encapsulated pancreatic islets. *Diabetologia* 45:159–173.
16. Qi M, et al. (2011) A recommended laparoscopic procedure for implantation of microcapsules in the peritoneal cavity of non-human primates. *J Surg Res* 168:e117–e123.
17. Jacobs-Tulleneers-Thevissen D, et al.; Beta Cell Therapy Consortium EU-FP7 (2013) Sustained function of alginate-encapsulated human islet cell implants in the peritoneal cavity of mice leading to a pilot study in a type 1 diabetic patient. *Diabetologia* 56:1605–1614.
18. Lutz J, et al. (1997) Measurement of oxygen tensions in the abdominal cavity and in the skeletal muscle using 19F-MRI of neat PFC droplets. *Oxygen Transport to Tissue XIX* eds Harrison DK, Delpy DT, (Springer, Boston), Vol 428, pp 569–572.
19. Klossner J, Kivisaari J, Niinikoski J (1974) Oxygen and carbon dioxide tensions in the abdominal cavity and colonic wall of the rabbit. *Am J Surg* 127:711–715.
20. Towell ME, Lysak I, Layne EC, Bessman SP (1976) Tissue oxygen tension in rabbits measured with a galvanic electrode. *J Appl Physiol* 41:245–250.
21. Goh F, Sambanis A (2011) *In vivo* noninvasive monitoring of dissolved oxygen concentration within an implanted tissue-engineered pancreatic construct. *Tissue Eng Part C Methods* 17:887–894.
22. Bourdel N, et al. (2007) Peritoneal tissue-oxygen tension during a carbon dioxide pneumoperitoneum in a mouse laparoscopic model with controlled respiratory support. *Hum Reprod* 22:1149–1155.
23. Klueh U, Frailey JT, Qiao Y, Antar O, Kreutzer DL (2014) Cell based metabolic barriers to glucose diffusion: Macrophages and continuous glucose monitoring. *Biomaterials* 35:3145–3153.
24. King A, Sandler S, Andersson A (2001) The effect of host factors and capsule composition on the cellular overgrowth on implanted alginate capsules. *J Biomed Mater Res* 57:374–383.
25. Johnson AS, Fisher RJ, Weir GC, Colton CK (2009) Oxygen consumption and diffusion in assemblages of respiring spheres: Performance enhancement of a bioartificial pancreas. *Chem Eng Sci* 64:4470–4487.
26. Dionne KE, Colton CK, Yarmush ML (1993) Effect of hypoxia on insulin secretion by isolated rat and canine islets of Langerhans. *Diabetes* 42:12–21.
27. Hals IK, Rokstad AM, Strand BL, Oberholzer J, Grill V (2013) Alginate microencapsulation of human islets does not increase susceptibility to acute hypoxia. *J Diabetes Res* 2013:374925.
28. Komatsu H, et al. (2017) Oxygen environment and islet size are the primary limiting factors of isolated pancreatic islet survival. *PLoS One* 12:e0183780.
29. Johnson AS, et al. (2011) Quantitative assessment of islets of Langerhans encapsulated in alginate. *Tissue Eng Part C Methods* 17:435–449.
30. Pepper AR, et al. (2015) A prevascularized subcutaneous device-less site for islet and cellular transplantation. *Nat Biotechnol* 33:518–523.
31. Pedraza E, Coronel MM, Fraker CA, Ricordi C, Stabler CL (2012) Preventing hypoxia-induced cell death in beta cells and islets via hydrolytically activated, oxygen-generating biomaterials. *Proc Natl Acad Sci USA* 109:4245–4250.
32. O'Sullivan ES, Vegas A, Anderson DG, Weir GC (2011) Islets transplanted in immunoisolation devices: A review of the progress and the challenges that remain. *Endocr Rev* 32:827–844.
33. Moya ML, Morley M, Khanna O, Opara EC, Brey EM (2012) Stability of alginate microbead properties in vitro. *J Mater Sci Mater Med* 23:903–912.
34. Darrabie MD, Kendall WF, Opara EC (2006) Effect of alginate composition and gelling cation on microbead swelling. *J Microencapsul* 23:613–621.
35. (2010) *Molecular Imaging: Principles and Practice* (People's Medical Publishing House, Shelton, CT).
36. Takahashi S, et al. (2012) Reversible off-on fluorescence probe for hypoxia and imaging of hypoxia-normoxia cycles in live cells. *J Am Chem Soc* 134:19588–19591.
37. Knox HJ, et al. (2017) A bioreducible N-oxide-based probe for photoacoustic imaging of hypoxia. *Nat Commun* 8:1794.
38. Cao F, Qiu Z, Li H, Lai P (2017) Photoacoustic imaging in oxygen detection. *Appl Sci* 7: 1262.
39. Carlin S, Humm JL (2012) PET of hypoxia: Current and future perspectives. *J Nucl Med* 53:1171–1174.
40. Krohn KA, Link JM, Mason RP (2008) Molecular imaging of hypoxia. *J Nucl Med* 49: 129S–148S.
41. Liu VH, Vassiliou CC, Imaad SM, Cima MJ (2014) Solid MRI contrast agents for long-term, quantitative in vivo oxygen sensing. *Proc Natl Acad Sci USA* 111:6588–6593.
42. Shi Y, et al. (2013) Mapping in vivo tumor oxygenation within viable tumor by 19F-MRI and multispectral analysis. *Neoplasia* 15:1241–1250.
43. Nöth U, et al. (1999) 19F-MRI in vivo determination of the partial oxygen pressure in perfluorocarbon-loaded alginate capsules implanted into the peritoneal cavity and different tissues. *Magn Reson Med* 42:1039–1047.
44. Nöth U, et al. (2004) In vivo determination of tumor oxygenation during growth and in response to carbogen breathing using 15C5-loaded alginate capsules as fluorine-19 magnetic resonance imaging oxygen sensors. *Int J Radiat Oncol Biol Phys* 60: 909–919.
45. Lemaire L, et al. (2013) Perfluorocarbon-loaded lipid nanocapsules as oxygen sensors for tumor tissue pO_2 assessment. *Eur J Pharm Biopharm* 84:479–486.
46. Dardzinski BJ, Sotak CH (1994) Rapid tissue oxygen tension mapping using 19F inversion-recovery echo-planar imaging of perfluoro-15-crown-5-ether. *Magn Reson Med* 32:88–97.
47. Janjic JM, Ahrens ET (2009) Fluorine-containing nanoemulsions for MRI cell tracking. *Wiley Interdiscip Rev Nanomed Nanobiotechnol* 1:492–501.
48. Ruiz-Cabello J, Barnett BP, Bottomley PA, Bulte JWM (2011) Fluorine (19F) MRS and MRI in biomedicine. *NMR Biomed* 24:114–129.
49. Ahrens ET, Flores R, Xu H, Morel PA (2005) In vivo imaging platform for tracking immunotherapeutic cells. *Nat Biotechnol* 23:983–987.
50. Hees PS, Sotak CH (1993) Assessment of changes in murine tumor oxygenation in response to nicotinamide using 19F NMR relaxometry of a perfluorocarbon emulsion. *Magn Reson Med* 29:303–310.
51. Zimmermann U, et al. (2000) Non-invasive evaluation of the location, the functional integrity and the oxygen supply of implants: ^{19}F nuclear magnetic resonance imaging of perfluorocarbon-loaded Ba^{2+}-alginate beads. *Artif Cells Blood Substit Immobil Biotechnol* 28:129–146.
52. Barnett BP, et al. (2011) Fluorocapsules for improved function, immunoprotection, and visualization of cellular therapeutics with MR, US, and CT imaging. *Radiology* 258:182–191.
53. Goh F, Long R, Jr, Simpson N, Sambanis A (2011) Dual perfluorocarbon method to noninvasively monitor dissolved oxygen concentration in tissue engineered constructs in vitro and in vivo. *Biotechnol Prog* 27:1115–1125.
54. Esteva A, et al. (2017) Dermatologist-level classification of skin cancer with deep neural networks. *Nature* 542:115–118.
55. LeCun Y, Bengio Y, Hinton G (2015) Deep learning. *Nature* 521:436–444.
56. Bahl M, et al. (2017) High-risk breast lesions: A machine learning model to predict pathologic upgrade and reduce unnecessary surgical excision. *Radiology* 286:810–818.
57. Daoud J, Rosenberg L, Tabrizian M (2010) Pancreatic islet culture and preservation strategies: Advances, challenges, and future outlook. *Cell Transplant* 19:1523–1535.
58. Goh F, Gross JD, Simpson NE, Sambanis A (2010) Limited beneficial effects of perfluorocarbon emulsions on encapsulated cells in culture: Experimental and modeling studies. *J Biotechnol* 150:232–239.
59. Schmieder AH, Caruthers SD, Keupp J, Wickline SA, Lanza GM (2015) Recent advances in ^{19}Fluorine magnetic resonance imaging with perfluorocarbon emulsions. *Engineering (Beijing)* 1:475–489.
60. Ahrens ET, Helfer BM, O'Hanlon CF, Schirda C (2014) Clinical cell therapy imaging using a perfluorocarbon tracer and fluorine-19 MRI. *Magn Reson Med* 72:1696–1701.